

Journal of Biomedical Optics

SPIEDigitalLibrary.org/jbo

Real-time photoacoustic imaging of prostate brachytherapy seeds using a clinical ultrasound system

Nathanael Kuo
Hyun Jae Kang
Danny Y. Song
Jin U. Kang
Emad M. Boctor

Real-time photoacoustic imaging of prostate brachytherapy seeds using a clinical ultrasound system

Nathanael Kuo,^a Hyun Jae Kang,^b Danny Y. Song,^c Jin U. Kang,^d and Emad M. Boctor^e

^aJohns Hopkins University, Department of Biomedical Engineering, 3400 North Charles Street, Baltimore, Maryland 21218

^bJohns Hopkins University, Department of Computer Science, 3400 North Charles Street, Baltimore, Maryland 21218

^cJohns Hopkins University, Department of Radiation Oncology, 401 North Broadway, Baltimore, Maryland 21231

^dJohns Hopkins University, Department of Electrical and Computer Engineering, 3400 North Charles Street, Baltimore, Maryland 21218

^eJohns Hopkins University, Department of Radiology, 3400 North Charles Street, Baltimore, Maryland 21218

Abstract. Prostate brachytherapy is a popular prostate cancer treatment option that involves the permanent implantation of radioactive seeds into the prostate. However, contemporary brachytherapy procedure is limited by the lack of an imaging system that can provide real-time seed-position feedback. While many other imaging systems have been proposed, photoacoustic imaging has emerged as a potential ideal modality to address this need, since it could easily be incorporated into the current ultrasound system used in the operating room. We present such a photoacoustic imaging system built around a clinical ultrasound system to achieve the task of visualizing and localizing seeds. We performed several experiments to analyze the effects of various parameters on the appearance of brachytherapy seeds in photoacoustic images. We also imaged multiple seeds in an *ex vivo* dog prostate phantom to demonstrate the possibility of using this system in a clinical setting. Although still in its infancy, these initial results of a photoacoustic imaging system for the application of prostate brachytherapy seed localization are highly promising. © 2012 Society of Photo-Optical Instrumentation Engineers (SPIE). [DOI: 10.1117/1.JBO.17.6.066005]

Keywords: prostate brachytherapy; photoacoustic imaging; clinical ultrasound; dynamic planning.

Paper 12033P received Jan. 13, 2012; revised manuscript received Apr. 5, 2012; accepted for publication Apr. 5, 2012; published online Jun. 4, 2012.

1 Introduction

Prostate cancer has long been a serious health concern around the world, with 241,740 estimated new cases and 28,170 estimated deaths in the United States alone throughout 2012.¹ Fortunately, there are several treatment options currently available, and one of the most popular is prostate brachytherapy (BT). This minimally invasive surgery involves the permanent implantation into the prostate of 50 to 100 grain-sized radioactive sources, known as seeds, that collectively emit a radiation dose distribution to eradicate cancerous tissue (see Fig. 1). BT has often been appreciated for good results in controlling cancer and reducing side effects while maintaining short recovery times.² However, the success of a BT operation critically depends on the placement of the radioactive seeds with respect to the prostate. While surgeons can nowadays achieve decent seed placement, current technology limits them from placing the seeds in the most optimal positions, which, in turn, has a negative impact on the quality of life for BT patients.

There are two factors that cause this failure from achieving optimal seed placement. The first is that, even in the most careful circumstances, seeds do not end up situated exactly in the positions where they are intended. In current day procedure, prior to the operation, the surgeon computes an optimal and patient-specific seed-placement plan to execute during the surgery. During execution, however, seeds inevitably deviate from the planned positions due to various causes, therefore leading to suboptimal results. These deviations could potentially be compensated by updating and re-optimizing the seed-placement plan

based on real-time position feedback of already implanted seeds, a process once referred to intraoperative treatment planning (ITP) but is now more precisely called dynamic planning (see Fig. 2).³ However, this leads to the second factor preventing optimal seed placement, in that there does not currently exist an imaging system that provides immediate seed-position feedback in the operating room (OR), therefore precluding dynamic planning. While transrectal ultrasound (TRUS) is commonly used to provide rough guidance for the surgeon in placing seeds, it has become generally accepted that current TRUS technology alone is insufficient to generate the seed position information required for dynamic planning due to its poor image quality.⁴

As a result, researchers have been investigating alternative imaging systems that would resolve this issue of intraoperatively visualizing and localizing seeds in relation to the prostate. These systems include TRUS-fluoroscopy,⁵⁻⁷ cone-beam computed tomography (CT),⁸ magnetic resonance imaging (MRI),⁹ and more, each of which has its strengths and weaknesses for this BT application. A review paper by Polo et al.¹⁰ provides a comprehensive overview of such alternative approaches. Nonetheless, photoacoustic imaging (PAI) has recently emerged as a promising imaging modality for various biomedical applications and may be particularly fitting for BT. This technology is centered on a physical phenomenon known as the photoacoustic effect, in which electromagnetic energy, such as pulsed light from a laser source, is absorbed by a target material, converted into acoustic energy through rapid thermoelastic expansion, and can consequently be detected with ultrasound transducers. PAI would be effective in localizing seeds due to the strong contrast it generates between seeds and tissue at certain wavelengths of

Address all correspondence to: Nathanael Kuo, Johns Hopkins University, Department of Biomedical Engineering, 3400 North Charles Street, Baltimore, Maryland 21218. Tel: +2149524318; E-mail: nkuo8@jhmi.edu

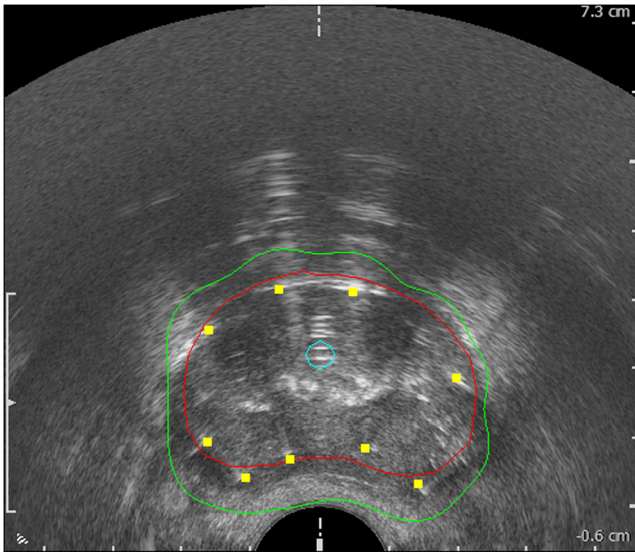


Fig. 1 Sample dosimetry to illustrate ultrasound-guided prostate brachytherapy. Yellow square dots represent the estimated seed positions, inner cyan contour represents estimated position of the urethra, middle red contour represents estimated position of the prostate, and outer green contour represents estimated radiation dose coverage given by the estimated seed positions.

light. It would also be practical for BT since it takes advantage of already-existing ultrasound equipment in the OR, thus reducing any additional burden on the surgeon. PAI would also be cost-effective, since it would not require any large imaging equipment such as a CT or MRI scanner, but only the addition of a laser.

There are other groups who have worked on photoacoustic imaging of metal needles,¹¹ BT seeds in chicken tissue,¹² and iodine seeds in bovine prostate tissue.¹³ However, we provide an alternative PAI system, validating it by imaging palladium seeds in dog prostate tissue, which is the standard animal model for the human prostate. We have presented initial results in previous conferences^{14,15} and extend that work in this paper. Although this research area is still in its infancy, we are excited

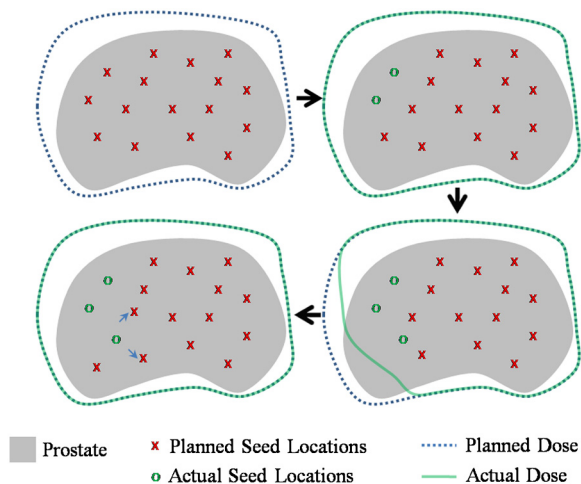


Fig. 2 Illustration of dynamic planning. Top left: Surgeon plans seed locations to give planned dose. Top right: Surgeon implants seeds so that actual seed locations match planned seed locations. Bottom right: An implanted seed deviates from planned location causing “cold spot.” Bottom left: Dynamic planning modifies future planned seed locations to compensate for deviations already present.

to present a PAI system and its initial results to demonstrate the possibility of applying PAI to BT.

2 Materials and Methods

2.1 Photoacoustic Imaging System Hardware

The hardware for our PAI system consists of three parts: (1) the laser; (2) the ultrasound system; and (3) the data acquisition device (see Fig. 3).

The laser we use is a neodymium-doped yttrium aluminum garnet (Nd:YAG) laser manufactured by Continuum, Inc., model Minilite II (Santa Clara, CA, USA). Its pulse repetition rate can be varied from 1 to 15 Hz, and the energy of the laser can also be adjusted from 0 to 50 mJ/pulse. The laser spot size can be altered by optics, but for our purposes, it is kept at the default beam diameter of 3 mm ($1/e^2$ full width). The wavelength is centered at 1064 nm, and this wavelength provides good contrast between the metallic seeds, which strongly absorb such light, and the soft tissue of the prostate, which does not.¹³ As far as human safety is concerned, the maximum permissible exposure at this wavelength is 100 mJ/cm². Finally, the pulse duration is approximately 5 ns, which well satisfies the thermal and stress confinement conditions for generating the photoacoustic effect efficiently.

The ultrasound system in this setup is the SonixRP produced by Ultrasonix Medical Corporation (Richmond, BC, Canada). It is a diagnostic ultrasound system packaged with an ultrasound research interface that allows some features for research purposes that are not available on a purely clinical system. We equipped this system with a standard 128-element 60-mm linear array transducer (model L14-5W). Note that all our ultrasound equipment is commercialized and approved for clinical use. This makes our setup rather distinct, since most other photoacoustic groups use customized ultrasound transducers rather than equipment that is already clinically approved.

The final piece is the data acquisition device, which is necessary to acquire photoacoustic images in real-time. Although

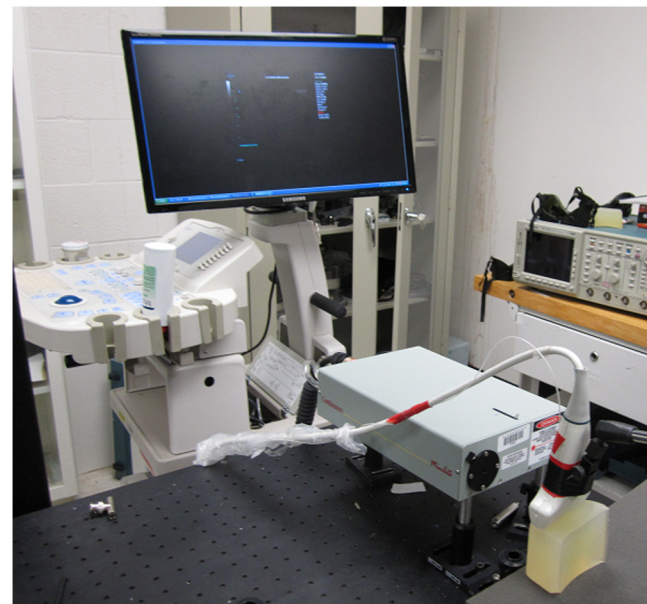


Fig. 3 Figure of photoacoustic imaging system setup. System is composed of laser (bottom right), ultrasound system (top left), and data acquisition device (not in view).

photoacoustic and ultrasonic data can both be acquired by ultrasound transducers, their acquisition processes are fundamentally different. In ultrasound, most images are acquired using focused beams transmitted along lines. After transmission, the signals received by the transducer elements are then combined in such a way as to tune to the area excited by the focused ultrasound beam (a process known as beamforming) to form a single line of data. The process repeats until all lines (generally, 128 lines, or however many elements there are in the transducer) are acquired to form one frame. On the other hand, in photoacoustic imaging, rather than exciting a single line, a single laser pulse may excite the whole field of view, implying that acquisition should be done frame-by-frame rather than line-by-line. Moreover, we are no longer interested in the post-beam-formed data of a single line but the raw pre-beam-formed data of the entire frame, which can then be reconstructed as we choose. Unfortunately, clinical ultrasound systems generally do not provide access to this level of data due to the lack of current clinical interest and the vast size of pre-beam-formed data that is generally collected. However, the Ultrasonix Medical Corporation recently made available the SonixDAQ, a data acquisition device that allows the acquisition of raw pre-beam-formed data in parallel to standard imaging. Our group initialized the development of this SonixDAQ module specifically for this application in collaboration with the University of Hong Kong and Ultrasonix. It supports 128 elements with 12-bit sampling along with external triggering for synchronous data acquisition. In addition, the SonixDAQ has 16-GB internal memory, a 40-MHz internal clock, and a USB port for transferring data.

Even with all these pieces of hardware at hand, they must also be synchronized to ensure proper imaging. To accomplish this task, we use the SonixRP to trigger the SonixDAQ, as the SonixDAQ is so designed to work with Ultrasonix ultrasound systems. We also used the same SonixRP signal to trigger the Minilite II. However, the unmodified signal from the SonixRP is incompatible with the Minilite II, so we built a monostable multivibrator circuit to transform the SonixRP impulse train trigger signal into the proper Minilite II TTL signal. Even so, there is a delay of approximately 150 μ s between the trigger signal and the actual firing of the laser because of the Q-switched nature of the Minilite II. We account for this by adding in software the same delay after the trigger signal before acquiring data with the SonixDAQ.

2.2 Real-Time Photoacoustic Imaging Software

Some software is also needed to acquire and reconstruct photoacoustic images in real-time.

While the SonixDAQ provides us the functionality of acquiring pre-beam-formed data, it only allows the user to download the data off the device after acquisition and does not provide real-time streaming of the data. To circumvent this limitation, we developed a software module we call the MUSiiC-DAQ-Server,¹⁶ which we incorporate into our larger software architecture known as MUSiiCToolkit.¹⁷ The MUSiiC-DAQ-Server is therefore a module that streams packets of data from the SonixDAQ and is created based on the software development kit (SDK) provided by Ultrasonix. The data is then communicated via the network using an extended version of OpenIGTLink,¹⁸ which we call OpenIGTLinkMUSiiC.¹⁹ The pre-beam-formed data is finally loaded into MATLAB by Mathworks (Natick, MA, USA) using the OpenIGTLink/MATLAB interface.

Once the data is loaded into MATLAB, we have several beam-forming and reconstruction algorithms available to generate photoacoustic images. While the standard delay-and-sum beam-forming algorithm is a popular option, we also utilized the one-step image reconstruction function for linear measurement surfaces provided in the photoacoustic simulation MATLAB toolbox known as k-Wave.²⁰ This reconstruction algorithm is based on the exact frequency-domain reconstruction formula provided by Xu et al. for thermoacoustic tomography,²¹ therefore generating in theory more accurate photoacoustic images than delay-and-sum. The resulting reconstruction is then envelope-detected, and the dynamic range compressed by a square root function to produce our final photoacoustic image.

2.3 Phantom Experiments

We performed several phantom experiments to analyze how our PAI system responds to various situations as applicable in BT, such as variations in laser parameters and variations in phantom setup. The seeds we used were decayed Palladium-103 seeds from Theragenics Corporation (Buford, GA, USA) encapsulated in titanium cylindrical shells 0.8 mm in diameter and 4.5 mm long implanted into gelatin from porcine skin. Due to the limited power of our laser, we image a single or, at most, a few seeds in these experiments. These numbers are not nearly sufficient for thorough validation, since dozens of seeds are implanted in an actual BT operation. However, the purpose of these experiments is not to thoroughly validate this PAI system but to provide an initial understanding of its capability and limits. A more thorough validation can then be provided given a more powerful laser.

The first two experiments involved imaging a single seed while varying laser parameters, which are the pulse repetition rate and the laser energy. The first experiment therefore involved acquiring a series of images by varying pulse repetition rate from 1 to 15 Hz with a step size of 1 Hz, keeping all other parameters constant. The second experiment involved varying the energy from 0 to 50 mJ/pulse with a step size of 10 mJ/pulse, likewise keeping all other parameters constant. Except for the particular parameter that is being studied, the standard settings for these parameters are: (1) a repetition rate of 10 Hz; (2) an energy of 10 mJ/pulse; (3) the seed implanted 1 cm deep with respect to the laser source; (4) the seed implanted 2 cm deep with respect to the linear transducer probe; and (5) the probe oriented perpendicular to the seed (see Fig. 4).

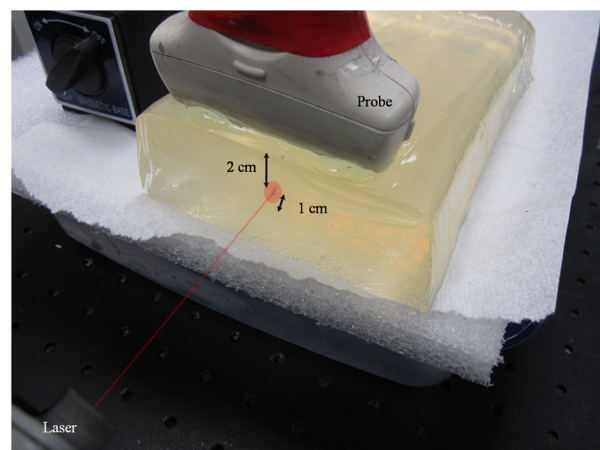


Fig. 4 Photograph of baseline setup. Note that laser is directed independently of transducer probe.

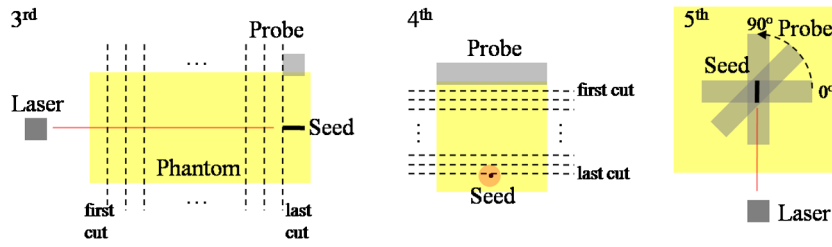


Fig. 5 Illustration of phantom parameter experiments. The left figure illustrates a side view of how the third experiment was conducted involving the parameter of the depth of the seed with respect to the laser. The center figure illustrates a front view of how the fourth experiment was conducted involving the parameter of the depth of the seed with respect to the probe. The right figure illustrates a top view of how the fifth experiment was conducted involving the parameter of the orientation of the probe with respect to the seed.

We also varied several parameters involving the phantom (see Fig. 5). Thus, the third experiment involved varying the depth of the seed implanted into the gelatin with respect to the laser, varying from 0 to 10 cm with a step size of 1 cm. This was done by starting with a large 10-cm slab of gelatin and gradually cutting away the gelatin down to 0 cm. In the fourth experiment, we varied the depth from the probe from 0 to 5 cm with a step size of 0.5 cm, again starting with a larger slab and cutting down to 0 cm. Finally, we also changed the orientation of the probe with respect to the seed, starting at 0 deg and ending at 90 deg with a step size of 15 deg. As with the laser parameters, we kept all other parameters at the standard settings indicated earlier with a few exceptions. The first exception is for the third experiment, that in addition to the standard data for the energy of 10 mJ/pulse, we also acquired data for the maximum energy of 50 mJ/pulse to see the effect of varying the depth of the seed with respect to the laser more clearly. The second exception is for the last experiment in that the seed was implanted 4 cm deep with respect to the laser, rather than the usual 1 cm deep, to make room for a full 90-deg probe rotation.

Finally, we also imaged a phantom consisting of an *ex vivo* dog prostate implanted with four seeds and again embedded in gelatin from porcine skin. This particular experiment was taken at a repetition rate of 10 Hz and at an intensity of 40 mJ/cm² using different but similar components to the previously described setup. Here we used the Surelite II, a larger more powerful sibling to the Minilite II, and the SonixCEP, a close kin to the SonixRP.

3 Results and Discussion

The results for the first experiment with varying pulse repetition rate are shown in Fig. 6. Note that the signal-to-noise ratio (SNR) after reconstruction remains relatively constant regardless of pulse repetition rate. This agrees with theory as the photoacoustic effect is independent of the pulse repetition rate. We can therefore expect that repetition rate would have little effect when applying PAI to BT as well. SNR here has been calculated as the difference of the maximum and minimum of the reconstructed data divided by the root mean squared of a constant region of interest representative of noise. Each data point is averaged over eight frames, and error bars represent standard deviation around this mean data point.

Likewise, the results for the second experiment with varying pulse energy are shown in Fig. 7. Note that SNR here is relatively linear with respect to laser pulse energy. This agrees with the theoretical equation:²⁰

$$p_0 = \Gamma \mu_a \Phi, \tag{1}$$

where p_0 is the initial pressure distribution caused by the photoacoustic effect, Γ is the Grüneisen parameter, which is a constant that relates absorbed light with the initial pressure, μ_a is the optical absorption coefficient, and Φ is the light fluence. Thus, as laser energy increases, the light fluence, Φ , increases

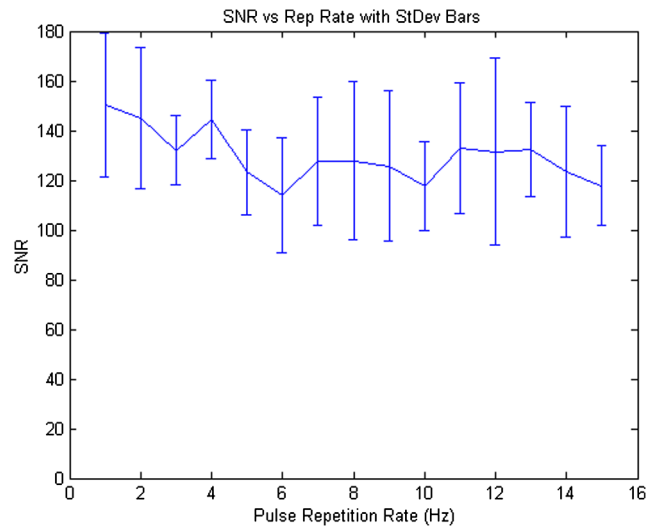


Fig. 6 Results of the first experiment showing signal-to-noise ratio with respect to repetition rate.

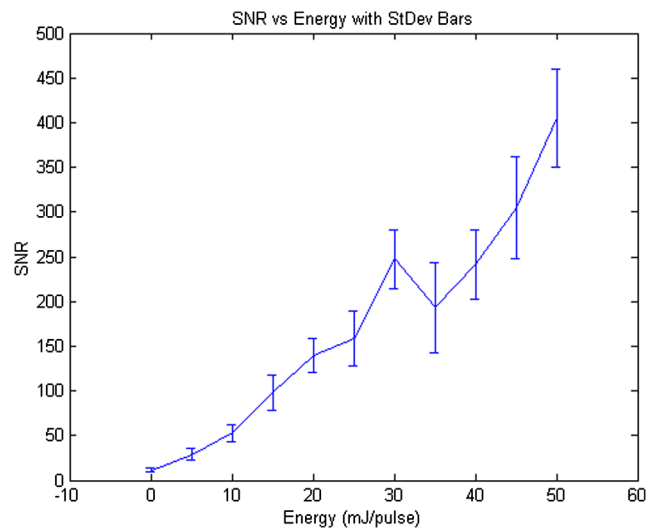


Fig. 7 Results of the second experiment showing signal-to-noise ratio with respect to energy.

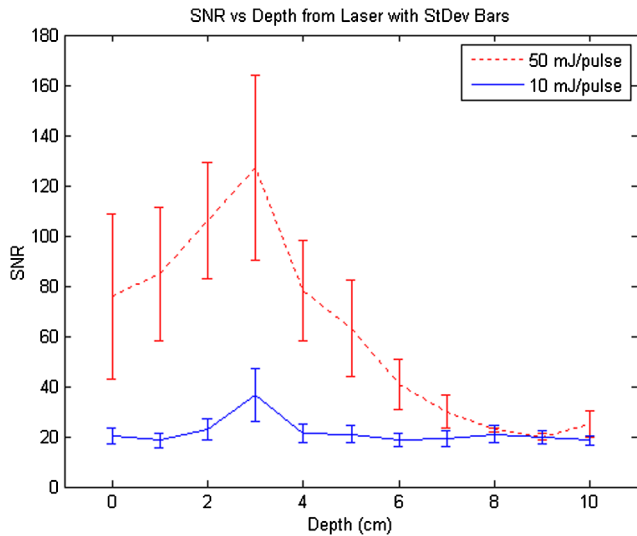


Fig. 8 Results of the third experiment showing signal-to-noise ratio with respect to depth of seed from laser.

proportionally while the Grüneisen parameter, Γ , and the absorption coefficient, μ_a , remain constant, causing a linear increase in the signal due to the linear increase in initial pressure distribution, p_0 . As a result, we can expect a linear increase in signal when increasing pulse energy in a BT experiment.

The results for the third experiment with varying seed depth from the laser are shown in Fig. 8. Here we see a roughly exponential decay in SNR for both the 10 mJ/pulse case and the 50 mJ/pulse case. This agrees with the theory of Beer’s Law that is applicable to PAI, which states:

$$I(z) = I_0 e^{-\mu_a z}, \quad (2)$$

where $I(z)$ is the light intensity as a function of the depth z , I_0 is the initial intensity, and μ_a is the optical absorption coefficient of the medium. However, in our experiment, note that the first few centimeters of depth (0 to 2 cm) do not correspond at all with exponential decay. This may be due to inevitable inconsistencies in laser spot alignment caused from cutting the gelatin phantom. Since the spot from our laser has a Gaussian intensity profile, signals with the laser spot centered on the seed will have higher SNR than those slightly misaligned, due to the relationship between intensity and signal seen previously. Inconsistent alignment would therefore cause inconsistencies as seen in the first few centimeters of our plot. However, it can be concluded that sufficient signal can be generated up to 5 cm (roughly the length from base to apex of a human prostate) using 10 mJ/pulse and up to 9 cm using the max energy of 50 mJ/pulse.

Figure 9 shows photoacoustic images from our fourth experiment with varying seed depth from the probe. In this experiment, SNR does not play as significant of a role, since signal related to depth can easily be accounted for using the time-gain control of the ultrasound system. However, note the shape of the seed in these photoacoustic images remains relatively the same. An ultrasound echo can also be seen below the actual location of the seed due to its closeness to the edge of the phantom (about 1 cm away). This again agrees with theory as the acoustic waves generated by the photoacoustic effect should reconstruct to the same shape regardless of its location with respect to the probe. Echoes also should be expected since the impedance mismatch at the edge of the phantom causes the ultrasound waves generated by the photoacoustic effect to reflect and eventually be detected by the probe. In addition, streaking artifacts are somewhat noticeable due to the finite length of the probe, whereas a complete and clean reconstructed image would require a probe of infinite length.

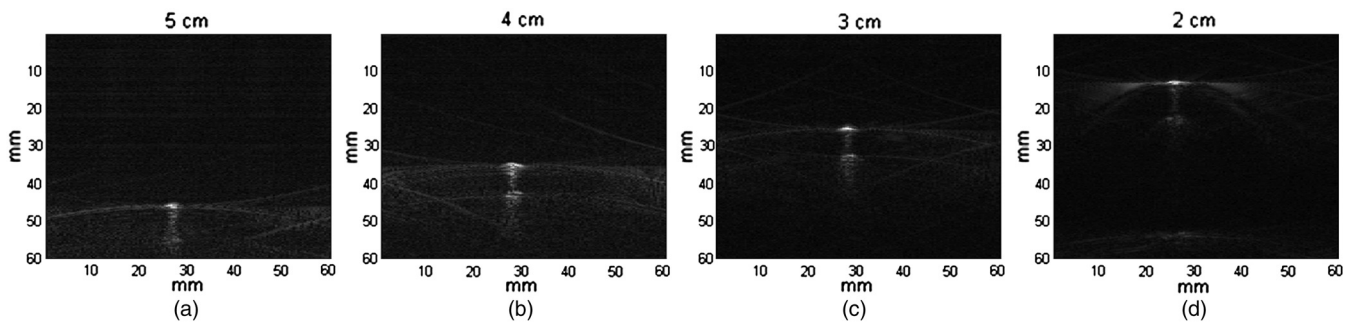


Fig. 9 Results of the fourth experiment showing images for (a) 5 cm, (b) 4 cm, (c) 3 cm, and (d) 2 cm depths of the seed from the ultrasound probe.

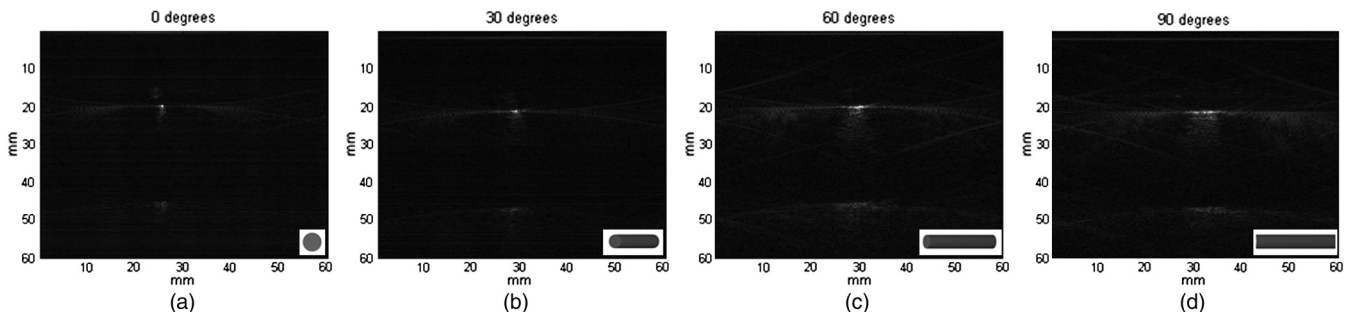


Fig. 10 Results of the fifth experiment showing images for (a) 0 deg, (b) 30 deg, (c) 60 deg, and (d) 90 deg of the probe oriented with respect to the seed.

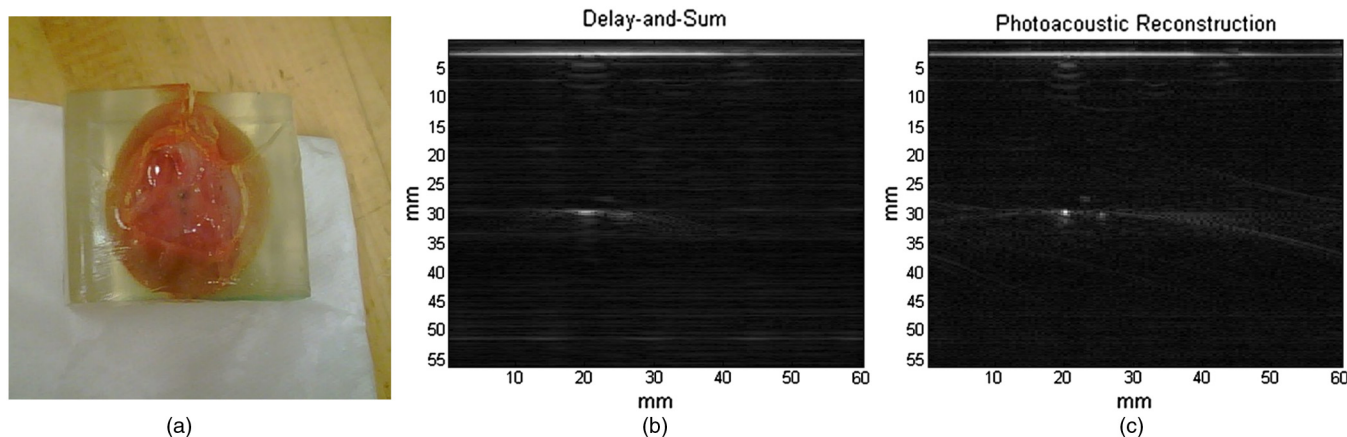


Fig. 11 Results from *ex vivo* phantom, including photograph (a), delay-and-sum image (b), and exact photoacoustic reconstruction image (c).

Figure 10 then shows photoacoustic images from our fifth experiment with varying seed orientation with respect to the probe. Note that the orientation of the seed is clearly seen in the reconstructed photoacoustic images, growing from a small axial cross-section in the 0-deg orientation to a long longitudinal cross-section in the 90-deg orientation of the cylindrical seed. As the orientations of the many seeds implanted in the prostate may differ in an actual BT procedure, this capability to visualize orientation differences may prove useful.

Finally, Fig. 11 shows the results of our final *ex vivo* dog prostate phantom experiment. Although four seeds were implanted in the prostate, only two seeds can be seen in this plane of view. Using standard delay-and-sum reconstruction, only one seed is visible. However, we can also take advantage of the linear geometry of the probe to apply to the same raw data the exact reconstruction formula provided in the k-Wave toolbox. The two seeds are consequently more visibly distinguishable.

4 Conclusion

In this paper, we present a PAI system that is capable of imaging prostate BT seeds. We study the capabilities of our system by varying laser and phantom parameters. Finally, we also show the results on an *ex vivo* dog prostate phantom to show the potential of applying this system to a clinical BT procedure.

However, it is obvious that there is much more to be done before this system could become a viable clinical system. For one, we need a more powerful laser system to enable the imaging of larger volumes and multiple seeds. Imaging of many seeds can be a potential issue in PAI as it is in ultrasound, since seeds closer to the transducer may obstruct the acoustic waves from seeds that are farther away. However, PAI has a distinct advantage over ultrasound since it captures more acoustic data using the full transducer aperture compared with the windowed aperture used in ultrasound, so image quality is not anticipated to suffer so significantly. Testing also needs to be done with a transrectal probe to ensure proper translation into the OR. Most probes used in BT have two transducers: one for transverse imaging and the other for longitudinal imaging. Functionality and scan conversion for both modes of operation should be made available for a complete PAI system. Light delivery of the laser to the prostate is also an issue that needs to be considered. While external radiation via the perineum would theoretically penetrate sufficiently deep to

image the prostate, it would be advantageous to incorporate optical fibers to ease light delivery. However, considering the laser intensity required to image the entire prostate, it would be challenging to develop a fiber setup to channel the laser power that is required. Finally, *in vivo* clinical studies should incorporate all these factors to eventually deliver a fully capable system into the OR.

Acknowledgments

We would like to extend our deepest thanks to Dr. Timothy Lippa from Johns Hopkins University Applied Physics Laboratory for lending us the Minilite II for these experiments. This work could not have been completed without his generosity. We also thank Dr. James Spicer from the Materials Science and Engineering Department at Johns Hopkins University and his student, Travis DeJournett, for their support and temporary use of the Surelite II.

References

1. R. Siegel, D. Naishadham, and A. Jemal, "Cancer statistics, 2012," *CA Cancer J. Clin.* **62**(1), 10–29 (2012).
2. A. V. Taira et al., "Long-term outcome for clinically localized prostate cancer treated with permanent interstitial brachytherapy," *Int. J. Rad. Oncol. Biol. Phys.* **79**(5), 1336–1342 (2011).
3. S. Nag et al., "Intraoperative planning and evaluation of permanent prostate brachytherapy: Report of the American Brachytherapy Society," *Int. J. Rad. Oncol. Bio. Phys.* **51**(5), 1422–1430 (2001).
4. B. H. Han et al., "Prostate brachytherapy seed identification on post-implant TRUS images," *Med. Phys.* **30**(5), 898–900 (2003).
5. L. Gong et al., "Ultrasonography and fluoroscopic fusion for prostate brachytherapy dosimetry," *Inter. J. Rad. Oncol. Biol. Phys.* **54**(5), 1322–1330 (2002).
6. Y. Su et al., "Seed localization and TRUS-fluoroscopy fusion for intraoperative prostate brachytherapy dosimetry," *Comp. Aid. Surg.* **12**(1), 25–34 (2007).
7. D. Y. Song et al., "Dynamic intraoperative dosimetry for prostate brachytherapy using a nonisocentric C-arm," *Brachytherapy* **10**(2), 98–106 (2011).
8. H. Westendorp et al., "Intraoperative adaptive brachytherapy of iodine-125 prostate implants guided by C-arm cone-beam computed tomography-based dosimetry," *Brachytherapy* **6**(4), 231–237 (2007).
9. A. V. D'Amico et al., "Real-time magnetic resonance imaging-guided brachytherapy in the treatment of selected patients with clinically localized prostate cancer," *J. Endour.* **14**(4), 367–370 (2000).
10. A. Polo et al., "Review of intraoperative imaging and planning techniques in permanent seed prostate brachytherapy," *Radio. Oncol.* **94**(1), 12–23 (2010).

11. J. Su et al., "Photoacoustic imaging of clinical metal needles in tissue," *J. Biomed. Opt.* **15**(2), 021309 (2010).
12. T. Harrison and R. J. Zemp, "Coregistered photoacoustic-ultrasound imaging applied to brachytherapy," *J. Biomed. Opt.* **16**(8), 080502 (2011).
13. J. Su et al., "Photoacoustic imaging of prostate brachytherapy seeds," *Biomed. Opt. Express* **2**(8), 2243–2254 (2011).
14. E. M. Boctor et al., "Prostate brachytherapy seed localization using combined photoacoustic and ultrasound imaging," presented at *Medical Imaging 2010, Ultrasonic Imaging, Tomography and Therapy*, San Diego, California, Poster Session Paper No. 7629-29, SPIE (14 February 2010).
15. N. Kuo et al., "Photoacoustic imaging of prostate brachytherapy seeds in ex vivo prostate," *Proc. SPIE* **7964**, 796409 (2011).
16. H. J. Kang et al., "Software framework of a real-time pre-beam-formed RF data acquisition of an ultrasound research scanner," *Proc. SPIE* **8320**, 83201F (2012).
17. P. J. Stolka, H. J. Kang, and E. M. Boctor, "The MUSiiC toolkit: modular real-time toolkit for advanced ultrasound research," *MIDAS J.*, 1–11 (2010).
18. J. Tokuda et al., "OpenIGTLink: an open network protocol for image-guided therapy environment," *Int. J. Med. Rob. Comp. Assist. Surg.* **5**(4), 423–434 (2009).
19. H. J. Kang, P. J. Stolka, and E. M. Boctor, "OpenITGLinkMUSiiC: a standard communications protocol for advanced ultrasound research," *MIDAS J.*, 1–12 (2011).
20. B. E. Treeby and B. T. Cox, "k-Wave: MATLAB toolbox for the simulation and reconstruction of photoacoustic wave fields," *J. Biomed. Opt.* **15**(2), 021314 (2010).
21. Y. Xu, D. Feng, and L. V. Wang, "Exact frequency-domain reconstruction for thermoacoustic tomography—I: planar geometry," *IEEE Trans. Med. Imaging* **21**(7), 823–828 (2002).